

# KTi<sub>2</sub>(PO<sub>4</sub>)<sub>3</sub> with Large Ion Diffusion Channel for High-Efficiency Sodium Storage

Jinzhi Sheng, Chen Peng, Yanan Xu, Haoying Lyu, Xu Xu,\* Qinyou An, and Liqiang Mai\*

To accommodate the decreasing lithium resource and ensure continuous development of energy storage industry, sodium-based batteries are widely studied to inherit the next generation of energy storage devices. In this work, a novel Na super ionic conductor type KTi<sub>2</sub>(PO<sub>4</sub>)<sub>3</sub>/carbon nanocomposite is designed and fabricated as sodium storage electrode materials, which exhibits considerable reversible capacity (104 mAh g<sup>-1</sup> under the rate of 1 C with flat voltage plateaus at ≈2.1 V), high-rate cycling stability (74.2% capacity retention after 5000 cycles at 20 C), and ultrahigh rate capability (76 mAh g<sup>-1</sup> at 100 C) in sodium ion batteries. Besides, the maximum ability for sodium storage is deeply excavated by further investigations about different voltage windows in half and full sodium ion cells. Meanwhile, as cathode material in sodium-magnesium hybrid batteries, the KTi<sub>2</sub>(PO<sub>4</sub>)<sub>3</sub>/carbon nanocomposite also displays good electrochemical performances (63 mAh g<sup>-1</sup> at the 230th cycle under the voltage window of 1.0–1.9 V). The results demonstrate that the KTi<sub>2</sub>(PO<sub>4</sub>)<sub>3</sub>/carbon nanocomposite is a promising electrode material for sodium ion storage, and lay theoretical foundations for the development of new type of batteries.

## 1. Introduction

Lithium ion batteries (LIBs) have been widely utilized in portable electronics and electric vehicles for decades due to their high energy density and long service life, making our life much more convenient.<sup>[1–4]</sup> However, LIBs can hardly satisfy the increasing market demand from the whole world for the shortage of lithium resource in the Earth's crust.<sup>[5–7]</sup> Nowadays, sodium ion batteries (SIBs), inheriting the similar intercalation chemistry of LIBs and avoiding the deficiency of lithium resource, are regarded as the potential alternatives of the next-generation energy storage system.<sup>[5–8]</sup> To accommodate

the larger ionic radius of Na<sup>+</sup> (1.02 Å, compared with 0.76 Å of Li<sup>+</sup>), one major challenge is the exploration of host electrode materials with larger ion diffusion channel and ions storage sites.

Comparing to the anode materials based on conversion reaction and alloying reaction with large volume change, intercalation-type materials provide more stable cycling stability, higher first cycle coulombic efficiency, and higher rate capability.<sup>[9–11]</sup> Among the intercalation-type materials, Na super ionic conductor (NASICON) can be considered as the ideal electrode materials for SIBs, owing to the high ionic conductivity from their open 3D framework.<sup>[12–17]</sup> Some of the transition metal phosphates, as a kind of typical NASICON material with good electrochemical activity, are being extensively studied.<sup>[10,14–17]</sup> NaTi<sub>2</sub>(PO<sub>4</sub>)<sub>3</sub> as a nontoxic and low-cost electrode material for SIBs has attracted much attention due to its flat

discharging plateau at an appropriate voltage of ≈2.1 V provided by the Ti<sup>3+</sup>/Ti<sup>4+</sup> conversion.<sup>[15–17]</sup> Compared to the lattice parameters of NaTi<sub>2</sub>(PO<sub>4</sub>)<sub>3</sub>, KTi<sub>2</sub>(PO<sub>4</sub>)<sub>3</sub> has a larger space along the c axis contributed by the larger ionic radius of K<sup>+</sup> (Figure S1, Supporting Information), which may provide a more capacious ion diffusion channel for the intercalation of Na<sup>+</sup>. Nevertheless, KTi<sub>2</sub>(PO<sub>4</sub>)<sub>3</sub> as a novel promising NASICON-type intercalation electrode material has been rarely investigated. Only by Han et al., KTi<sub>2</sub>(PO<sub>4</sub>)<sub>3</sub> was studied as anode materials for potassium ion batteries and SIBs, but the rate and cycling performances still need to be greatly improved.<sup>[18,19]</sup>

Recently, magnesium ion batteries (MIBs) have drawn increasing attention due to the high theoretical volumetric capacity of Mg (3833 mAh cm<sup>-3</sup> vs 2061 mAh cm<sup>-3</sup> of Li) without dendrites growth.<sup>[20–22]</sup> However, further development of MIBs has been limited by the narrow scope of optional cathode materials arising from the difficulty of the reversible storage of Mg<sup>2+</sup>.<sup>[22,23]</sup> In order to overcome the difficulty, lithium-magnesium hybrid batteries as a novel concept has been put forward by combining the Li storage cathode material with the Mg metal anode, which has aroused extensive attention, while it still suffers from the high cost of lithium.<sup>[24–26]</sup> In the same way, using sodium instead of lithium can obtain good results.<sup>[27,28]</sup> In addition to the application as anode in SIBs, KTi<sub>2</sub>(PO<sub>4</sub>)<sub>3</sub> is also a potential cathode material for

J. Z. Sheng, C. Peng, Y. N. Xu, H. Y. Lyu, Dr. X. Xu, Prof. Q. Y. An, Prof. L. Q. Mai  
State Key Laboratory of Advanced Technology for Materials Synthesis and Processing  
International School of Materials Science and Engineering  
Wuhan University of Technology  
Luoshi Road 122, Wuhan 430070, P. R. China  
E-mail: xuxu@whut.edu.cn; mlq518@whut.edu.cn  
Prof. L. Q. Mai  
Department of Chemistry  
University of California  
Berkeley, CA 94702, USA

DOI: 10.1002/aenm.201700247



**Figure 1.** Schematic illustration of the formation of the  $\text{KTi}_2(\text{PO}_4)_3$  based products.

sodium-magnesium hybrid batteries (SMHBs) owing to the suitable discharging center ( $\approx 1.3$  V vs  $\text{Na}^+/\text{Mg}$ ).

Herein, we report a carbon-coated  $\text{KTi}_2(\text{PO}_4)_3$  nanoparticle composite synthesized via a facile co-precipitation method followed by the annealing process. As a novel NACISON-type intercalation electrode materials for SIBs, the carbon-coated  $\text{KTi}_2(\text{PO}_4)_3$  nanoparticle composite exhibits ultrahigh rate capability ( $76 \text{ mAh g}^{-1}$  at  $100 \text{ C}$ ) and excellent high-rate cycling stability (about 74.2% capacity retention after 5000 cycles at  $20 \text{ C}$ ). The desirable electrochemical performances of this composite are contributed by the fine particle size and appropriate carbon coating, resulting in the shortened ion diffusion path and enhanced electronic conductivity. Furthermore, we also apply the  $\text{KTi}_2(\text{PO}_4)_3$ /carbon composite in the SMHBs and obtain

good performances, which opens up a new train of thoughts for the extensive application of intercalation materials in various energy storage systems.

## 2. Results and Discussions

As a typical synthesis process (Figure 1), the  $\text{KTi}_2(\text{PO}_4)_3$  precursor was obtained by a co-precipitation method. Followed by annealing the precursor in air, the pure  $\text{KTi}_2(\text{PO}_4)_3$  nanoparticles (KTP) were obtained. After mechanical stirring KTP with graphene, the  $\text{KTi}_2(\text{PO}_4)_3$ /graphene composite (KTP/G) was fabricated. The  $\text{KTi}_2(\text{PO}_4)_3$ /carbon composite (KTP/C) was constructed by annealing the precursor in argon. The X-ray diffraction (XRD) pattern of the  $\text{KTi}_2(\text{PO}_4)_3$  precursor shows no obvious diffraction peak, indicating an amorphous phase (Figure S2a, Supporting Information). The precursor exhibits a bulk morphology attached by some nanoparticles (Figure S2b, Supporting Information). According to the XRD patterns of the obtained three samples (Figure 2a), all of them show high crystallinity degree. The diffraction peaks of each pattern are indexed to the rhombohedral phase  $\text{KTi}_2(\text{PO}_4)_3$  (JCPDS No. 01-079-1880), indicating the pure phase of the three samples. The carbon phases are not observed in the XRD patterns due to their small content and low crystallinity degree. To confirm the morphologies of

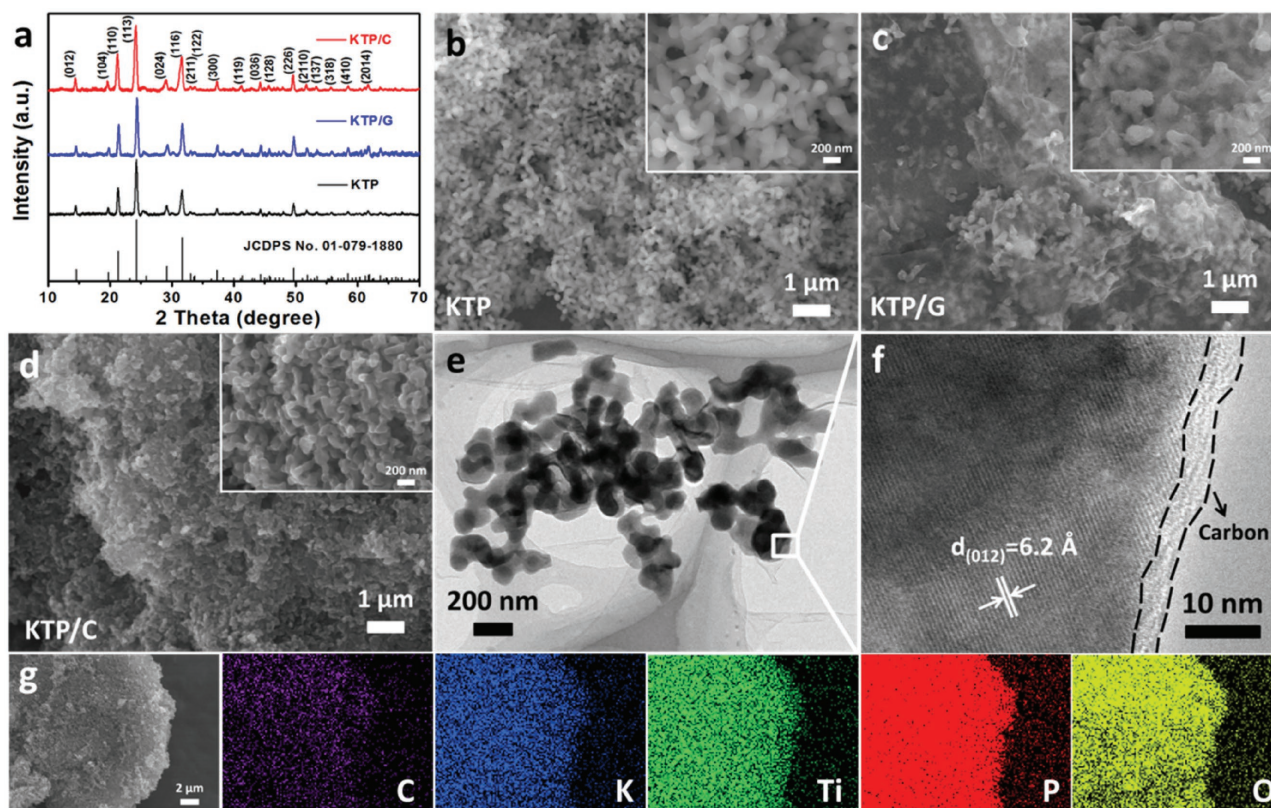


**Figure 2.** a) XRD patterns of KTP, KTP/G, and KTP/C; SEM images of b) KTP, c) KTP/G, and d) KTP/C; e) TEM and f) HRTEM images of KTP/C; and g) EDS-mapping of KTP/C.

these samples, scanning electron microscopy (SEM) was carried out. The KTP sample is constructed by uniform nanoparticles in diameter of 100–200 nm (Figure 2b). After mechanical stirring with graphene, the surface of the KTP nanoparticles was wrapped by the graphene, and the morphology of these nanoparticles remained unchanged (Figure 2c). The KTP/C sample was also made up of nanoparticles, which are smaller than the size of the KTP sample. Besides, slight aggregation was observed, which may be caused by the mutual adsorption of carbon (Figure 2d). The transmission electron microscopic (TEM) image indicates that the KTP/C nanoparticles are solid (Figure 2e). When using higher magnification to observe this sample, obvious lattice fringes with a distance of  $\approx 6.2$  Å confirm the existence of the (012) lattice plane of  $\text{KTi}_2(\text{PO}_4)_3$  (Figure 2f). An amorphous layer also finely coated on the surface of the nanoparticle was obviously observed, corresponding to the carbon layer in KTP/C. To investigate the element distribution in KTP/C, the energy dispersive spectrometer (EDS) was measured and shows the uniform distribution of C, K, Ti, P, and O, which further indicates the existence of the carbon phase (Figure 2g).

In order to further obtain the surface information of the three samples, Brunauer–Emmett–Teller (BET) measurement was taken and shown in Figure S3 (Supporting Information). The BET surface areas of KTP, KTP/G, and KTP/C are 13.8, 11.4, and  $24.9 \text{ cm}^3 \text{ g}^{-1}$ , respectively. And according to the pore size distribution curves in the inset figures, all the three samples have no obvious porous structure. The thermogravimetry (TG) curves of KTP/G and KTP/C are obtained to detect the carbon content in the samples (Figure S4, Supporting Information). The weight losses of 4.72% and 3.06% occur in KTP/G and KTP/C from 400 to 600 °C, respectively, corresponding to the relevant carbon content in each sample. The weight loss of 3.91% in KTP/G is mainly caused by the evaporation of absorbed water and the thermal decomposition of functional groups on graphene.<sup>[29,30]</sup> To confirm whether the carbon content is controllable, we have washed the precursor by ethanol for 0 and 5 times for comparison, and the TG-differential scanning calorimetry (DSC) results are exhibited in Figure S5 (Supporting Information). The weight loss appears at 400–600 °C in both of the two samples, corresponding to the oxidation of the carbon phase. The carbon content of 4.07 wt% is observed in the sample without washing, and the carbon content of 1.79 wt% is observed in the sample with five times washing. The result indicates that the organics can be partially eliminated by washing using ethanol, confirming that the carbon content in KTP/C sample is controllable.

The electrochemical performances of the three samples are obtained by assembling them in a 2016 coin cell as the cathode, combining with a sodium metal as the anode. There are two obvious peaks shown in the cyclic voltammetry (CV) curve of KTP/C tested under a voltage window of 1.4–3.0 V, which is tested after the cell cycled to a stable state (Figure 3a). The cathodic peak at 2.04 V corresponds to the  $\text{Na}^+$  intercalation process, and the anodic peak at 2.25 V corresponds to the  $\text{Na}^+$  deintercalation process. The charge–discharge curves of the three samples are also obtained after the cells cycled to a stable state at the rate of 1 C (1 C corresponds to  $128 \text{ mA g}^{-1}$ , referring to the theoretical capacity of  $\text{KTi}_2(\text{PO}_4)_3$ ) (Figure 3b).

Flat plateaus at  $\approx 2.1$  V can be observed in the KTP/C sample, indicating a stable and reversible electrochemical reaction process. The capacity of KTP/C reached  $104 \text{ mAh g}^{-1}$ , which is much higher than that of the KTP ( $22 \text{ mAh g}^{-1}$ ) and KTP/G ( $83 \text{ mAh g}^{-1}$ ). The KTP/G sample also shows the plateau at  $\approx 2.1$  V but is accompanied by obvious polarization, and the plateaus can hardly be seen in the pure KTP sample. Comparing to the cycling performance of the three samples at 5 C (Figure 3c), the KTP/C sample also shows the highest capacity. It obtains  $\approx 60 \text{ mAh g}^{-1}$  in the first cycle, and the capacity increases to  $\approx 96 \text{ mAh g}^{-1}$  after 100 cycles, which may be due to the activated process of the electrode.<sup>[31]</sup> After cycling for 1200 times, the KTP/C sample still maintains a reversible capacity of more than  $90 \text{ mAh g}^{-1}$ . However, the capacity of the KTP/G sample only reaches  $\approx 10 \text{ mAh g}^{-1}$  in the initial cycles, and increases to  $\approx 70 \text{ mAh g}^{-1}$  after  $\approx 1000$  cycles. This activated process is slower than that of KTP/C, mainly due to the nonuniform and weaker carbon compositing that leads to the tardiness of the active site spreading. The capacity of pure KTP sample only increases to  $\approx 12 \text{ mAh g}^{-1}$  after  $\approx 700$  cycles and keeps stable in the following 500 cycles.

The rate capabilities of these samples were tested under the rate ranging from 1 to 100 C after the cells cycled to a stable state (Figure 3d). The KTP/C sample obtains a relatively high capacity of  $\approx 104 \text{ mAh g}^{-1}$  at 1 C, and the capacity remains a large proportion under a high rate of 50 C. Remarkably, even at an ultrahigh rate of 100 C, it still obtains a high capacity of  $\approx 76 \text{ mAh g}^{-1}$ , where the charge process can be completed within 36 s. The capacity can also recover back to  $\approx 100 \text{ mAh g}^{-1}$  after the ultrahigh current pulse, showing a high reversibility. Under the low rates, the KTP and KTP/G sample shows similar performances with the previous results. However, when the charging–discharging rate rises to more than 50 C, the capacity rapidly decreases to almost zero. The charge–discharge curves of KTP/C under different rates (Figure 3e) show flat plateaus when the rate is lower than 20 C. With the rate increasing, the polarization phenomenon becomes more obvious. The ultralong cycling performance of KTP/C is also obtained (Figure 3g). Under the rate of 20 C, the initial capacity reaches  $\approx 60 \text{ mAh g}^{-1}$ , and increases to  $\approx 93 \text{ mAh g}^{-1}$  after 200 cycles. After 5000 cycles, the capacity still remains  $69 \text{ mAh g}^{-1}$ , reaching 74.2% of the highest capacity during the cycling, demonstrating the excellent cycling stability at high rate.

To examine the electrochemical kinetics behavior of  $\text{Na}^+$  ions in KTP/C, the galvanostatic intermittent titration technique (GITT) was measured to estimate the diffusion coefficient of  $\text{Na}^+$  ( $D_{\text{Na}^+}$ ). As shown in Figure S6 (Supporting Information), the GITT data of the second cycle were collected with a current flux of  $10 \text{ mA g}^{-1}$  in an interval of 5 min, interrupted by a relaxation for 10 min to get its steady-state voltages. The KTP/C shows a discharge capacity of  $124 \text{ mAh g}^{-1}$ , nearly corresponding to the insertion of 2  $\text{Na}^+$  per formula (based on the theoretical capacity of  $128 \text{ mAh g}^{-1}$  calculated by Equation (S1) of the Supporting Information). The  $D_{\text{Na}^+}$  was calculated based on the GITT curves for the KTP/C as a function of voltage using Equation (S2) of the supporting information. In the discharge process, the  $D_{\text{Na}^+}$  values are determined to be  $4.213 \times 10^{-13}$  to  $5.797 \times 10^{-15} \text{ m}^2 \text{ s}^{-1}$ , which is a relatively high value among the sodium storage materials.

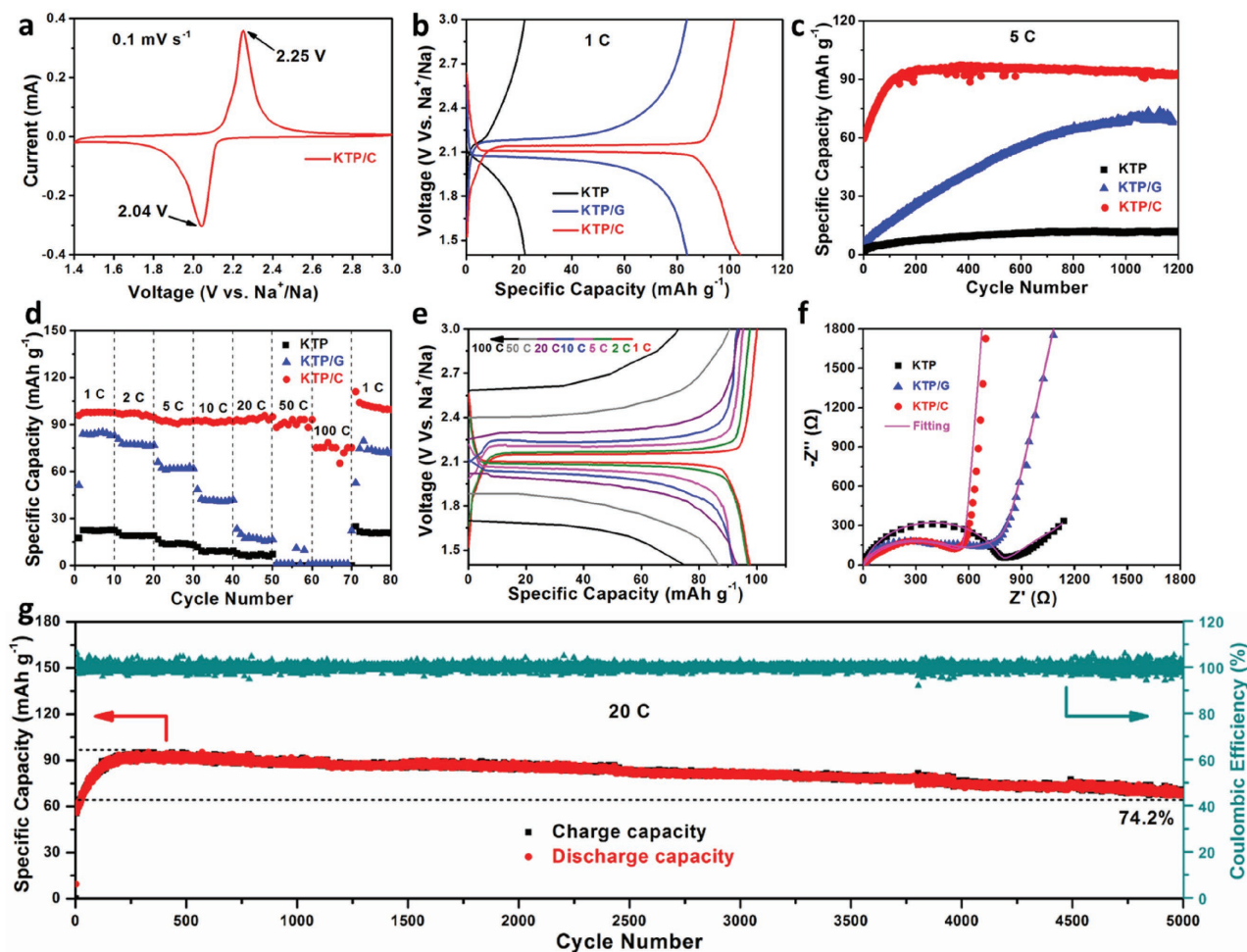


**Figure 3.** a) Cyclic voltammogram curve of KTP/C at a scan rate of  $0.1 \text{ mV s}^{-1}$ ; b) charge–discharge curves of KTP, KTP/G, and KTP/C at the rate of 1 C; c) cycling performance of KTP, KTP/G, and KTP/C at the rate of 5 C; d) rate performances of KTP, KTP/G, and KTP/C; e) charge–discharge curves of KTP/C at different rates; f) electrochemical impedance spectra of KTP, KTP/G, and KTP/C; and g) long cycling performance of KTP/C at the rate of 20 C.

To investigate the electronic conductivity of the three samples, the electrochemical impedance spectra (EIS) were measured (Figure 3f). The Nyquist plots show that the charge transfer resistance ( $R_{ct}$ ) of KTP/C ( $516.1 \Omega$ ) is much lower than that of KTP/G ( $680.2 \Omega$ ) and KTP ( $765.8 \Omega$ ). The detailed fitting data are displayed in Table S1 (Supporting Information). These results indicate that the KTP/C sample possesses higher electronic conductivity, which may be the main reason of its better performances than the other two samples. In addition, combining with the previous material characterization results, the uniform carbon coating and the larger specific surface area may also contribute to the superior performances of KTP/C.

The valence state changes of the elements in KTP/C were confirmed by the X-ray photoelectron spectroscopy (XPS) measurement. When the sample is charged to 3 V, the binding energy of the Ti  $2p_{3/2}$  and  $2p_{1/2}$  peaks is observed at  $\approx 458.8$  and  $\approx 465.8$  eV, respectively, corresponding to the  $\text{Ti}^{4+}$  (Figure S7a, Supporting Information).<sup>[32,33]</sup> When the sample is discharged to 1.4 V, two new peaks occur on the smaller binding energy side of the initial peak positions (Figure S7b, Supporting Information). After fitting, the Ti  $2p_{3/2}$  spectrum can be deconvoluted

into two peaks at 457.4 and 459.2 eV, which are ascribed to the state of  $\text{Ti}^{2+}$  and  $\text{Ti}^{4+}$ , respectively. The Ti  $2p_{1/2}$  spectrum can also be deconvoluted into two peaks at 462.9 and 464.7 eV, corresponding to the state of  $\text{Ti}^{2+}$  and  $\text{Ti}^{4+}$ , respectively.<sup>[34,35]</sup> These results demonstrate that part of Ti was reduced after  $\text{Na}^+$  intercalation.

Although we have strongly improved the performances of  $\text{KTi}_2(\text{PO}_4)_3$  and obtained superior results, there is still a distance away from the industrialization of this material for its relatively high voltage at  $\approx 2.1$  V, which results in the low energy density of full cells. Thus, the maximum sodium storage ability of  $\text{KTi}_2(\text{PO}_4)_3$  should be further excavated. The KTP/C sample was tested under different voltage windows in half and full sodium ion cells. When ranging the voltage from 0.01 to 1.4 V, the KTP/C obtains a capacity of  $\approx 150 \text{ mAh g}^{-1}$  at 5 C during the first discharging process (Figure S8a, Supporting Information). Part of the capacity is contributed by the formation of the solid electrolyte interphase (SEI) layer.<sup>[36,37]</sup> The charging capacity decreases to  $\approx 60 \text{ mAh g}^{-1}$  in the second cycle with a slope plateau at  $\approx 0.45$  V, and keeps stable in the following discharging process, which represents the reversible capacity

under this voltage window. After 3000 cycles, the sample still remains a capacity over  $40 \text{ mAh g}^{-1}$  (Figure S8b, Supporting Information), demonstrating the utilizability of the low voltage plateau. The voltage window 0.01–3.0 V containing the above two ranges is also measured to further study the properties of  $\text{KTi}_2(\text{PO}_4)_3$ . The discharging capacity of the first cycle is  $\approx 200 \text{ mAh g}^{-1}$  at 1 C, while the first charging capacity reaches  $\approx 185 \text{ mAh g}^{-1}$  (Figure S8c, Supporting Information). The extra discharging capacity in the initial cycles is caused by the formation of SEI layer (Figure S8d, Supporting Information). After 100 cycles,  $\approx 150 \text{ mAh g}^{-1}$  is maintained, also indicating a good cycling stability. The unchanged plateaus in charge–discharge curves at the 100th cycle confirm an intercalation reaction of KTP/C under the voltage window of 0.01–3.0 V. On account of that lower voltage provided in anodes will contribute to higher voltage in full cells, the results above show great potential of KTP/C when applied as an anode with high energy density.

It is well known that the sodium metal is not a safe material as the SIBs anode due to the dendrite growth. Thus, applying the KTP/C in the full cell sodium ion battery is of great importance. We chose the carbon-coated NASICON-type

$\text{Na}_3\text{V}_2(\text{PO}_4)_3$  (NVP/C) with a flat plateau at  $\approx 3.4 \text{ V}$  (vs  $\text{Na}^+/\text{Na}$ ) as the cathode material to assemble the full cell with KTP/C, and tested the full cells under different voltage windows. The XRD pattern (Figure S9a, Supporting Information) of NVP/C shows a pure phase of  $\text{Na}_3\text{V}_2(\text{PO}_4)_3$  (JCPDS No. 53-0018), and the SEM images (Figure S9b, Supporting Information) exhibit a bulk structure. Because KTP/C is our research object, we added excess amount of NVP/C to construct the full cell. First, the performances based on the same voltage window (1.4–3.0 V) of KTP/C with previous measurements were investigated (Figure 4a–c). Both of the NVP/C sample and KTP/C sample exhibit flat plateaus at  $\approx 3.4$  and  $\approx 2.1 \text{ V}$ , respectively. When testing the full cell from 0.5 to 2.0 V, a new flat plateau at  $\approx 1.25 \text{ V}$  is observed. The capacity provided by this plateau reaches  $\approx 68 \text{ mAh g}^{-1}$ , and remains more than  $60 \text{ mAh g}^{-1}$  after 300 cycles. In the first few cycles, the capacity experiences an increasing process, which may be due to the activate process of KTP/C.<sup>[34,35]</sup> Besides the plateau in the higher voltage, the KTP/C also shows a slope plateau at  $\approx 0.5 \text{ V}$ . To investigate the performances contributed by this plateau, the full cell voltage window of 2.5–3.4 V was chosen. The initial discharging

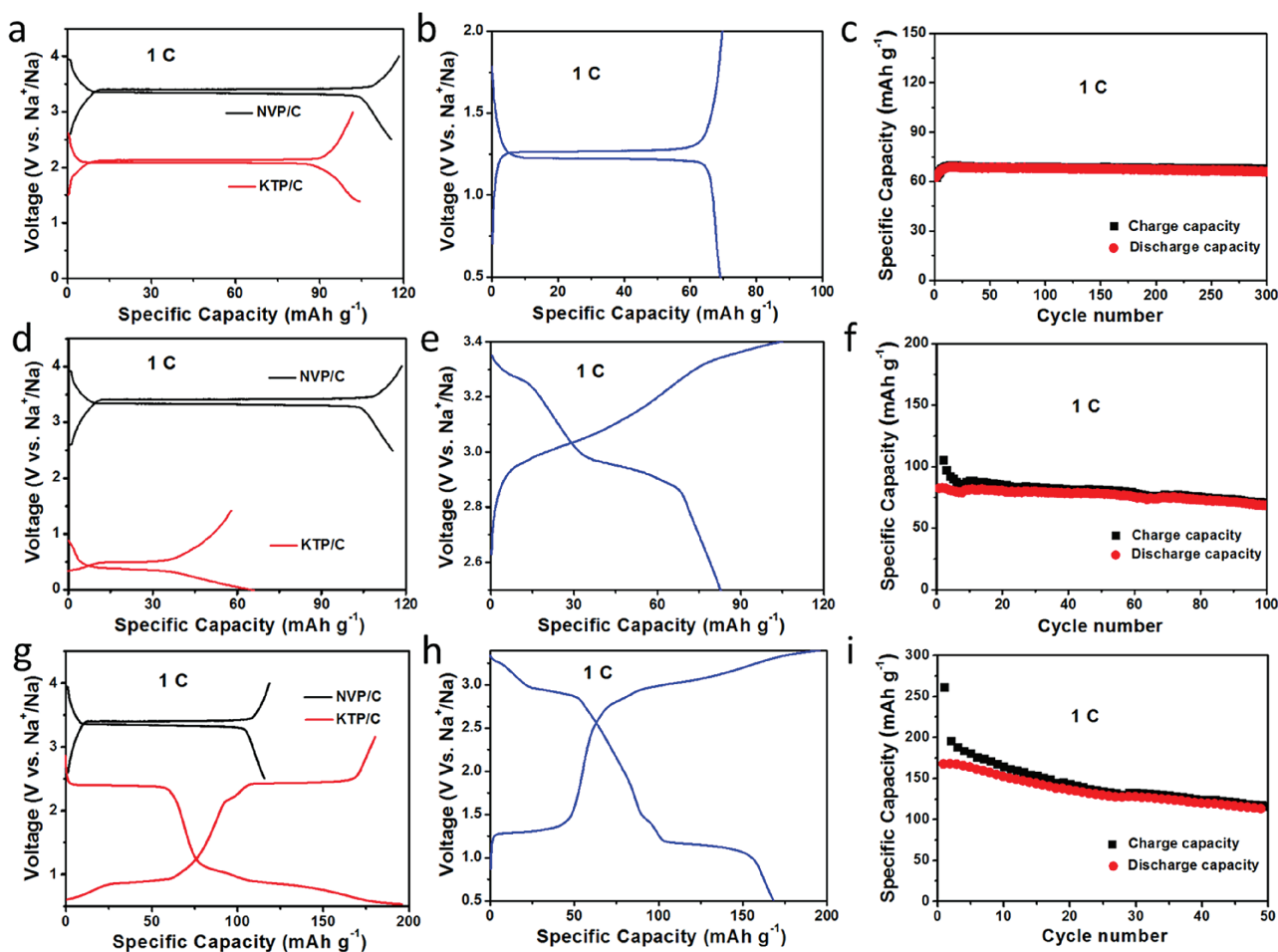


**Figure 4.** Charge–discharge curves of KTP/C under the voltage windows of a) 1.4–3.0 V, d) 0.01–1.4 V, and g) 0.01–3.0 V combined with the charge–discharge curves of NVP/C under a voltage window of 2.5–4.0 V in the half cells; charge–discharge curves of the NVP/C//KTP/C full cell under the voltage windows of b) 0.5–2.0 V, e) 2.5–3.4 V, h) and 0.5–3.4 V; cycling performances of the NVP/C//KTP/C full cell under the voltage windows of c) 0.5–2.0 V, f) 2.5–3.4 V, and i) 0.5–3.4 V.

capacity reaches  $\approx 83 \text{ mAh g}^{-1}$  and remains  $\approx 72 \text{ mAh g}^{-1}$  after 100 cycles with a stable plateau at  $\approx 3.0 \text{ V}$ . The low coulombic efficiency of the initial cycles is caused by the formation of the SEI layer.<sup>[34,35]</sup> Notably, the reversible capacity of low plateau confirms the structure stability under the low voltage cycling, indicating the absence of conversion reaction.<sup>[34,35]</sup> The performances combining both two plateaus are also obtained using the full cell voltage window of 0.5–3.4 V. The initial discharging capacity reaches  $\approx 165 \text{ mAh g}^{-1}$  and remains more than  $100 \text{ mAh g}^{-1}$  after 50 cycles. The rate capability under this voltage window was also measured (Figure S10, Supporting Information). When the rate reached 20 C, the capacity of  $\approx 50 \text{ mAh g}^{-1}$  was maintained. After the rate returned back to 1 C, more than  $150 \text{ mAh g}^{-1}$  capacity could be recovered. The low voltage plateau of KTP/C provides a higher discharge plateau of the full cell, which shows much higher energy density. Thus, it is further demonstrated that the KTP/C is a promising anode material for SIBs.

For the high theoretical volumetric capacity of Mg ( $3833 \text{ mAh cm}^{-3}$  vs that of Li  $2061 \text{ mAh cm}^{-3}$ ) and no dendritic growth, the Mg metal anode based SMHBs become an energy storage system with great potential of industrialization. Owing to a suitable plateau voltage (below 2 V vs  $\text{Mg}^{2+}/\text{Mg}$ , oxygen evolution reaction between the electrode and the battery shell may occur under this voltage) of KTP/C, it may obtain good performance applying the KTP/C in the SMHBs, and the operating mechanism is illustrated in Figure 5a. From the charge–discharge curves of the SMHB at different cycles (Figure 5b), a capacity of  $\approx 63 \text{ mAh g}^{-1}$  is obtained at the 230th cycle under the voltage window of 1.0–1.9 V. The discharging voltage plateau is  $\approx 1.3 \text{ V}$ , and the charging voltage plateau locates at  $\approx 1.5 \text{ V}$ . These curves also show a slope plateau corresponding to the same reaction of KTP/C at 2.1 V in the half cell sodium ion battery. The cycling performance of the SMHB (Figure 5c) exhibits a low initial capacity, and the capacity increases throughout  $\approx 230$  cycles, which may also be due to the activation of  $\text{KTi}_2(\text{PO}_4)_3$ . The low coulombic efficiency in the initials few cycles may be caused by the activation of the electrolyte.<sup>[27]</sup> Although the SMHB testing technique is not fully developed, our study in successfully applying the KTP/C sample in this advanced energy storage system is still of great significance.

Based on the results exhibited above, the KTP/C sample shows obvious advantages in sodium ion storage, which is mainly due to three aspects: (1) the NASICON-type crystalline structure provides broad and large ion diffusion channels;<sup>[12–14]</sup> (2) the reduced nanoscale particle size provides shortened ion diffusion path;<sup>[38]</sup> (3) the uniform carbon layer coating, which owns stronger combination with the active materials than that of graphene, provides high electronic transformation synergizing

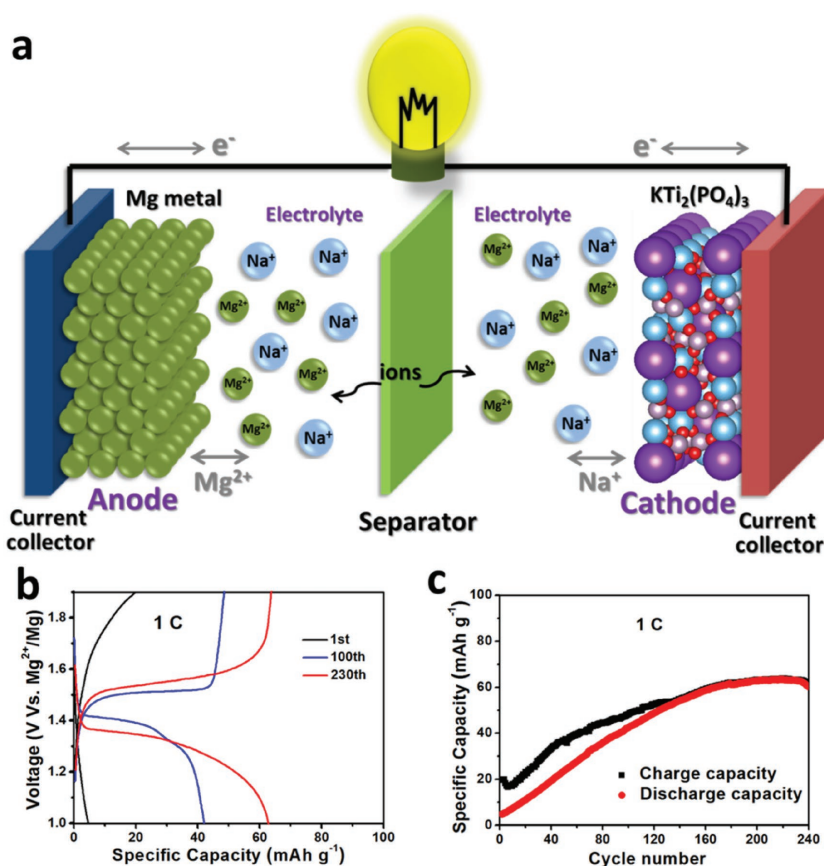


**Figure 5.** a) Schematic illustration of the SMHBs using KTP/C as cathode material; b) charge–discharge curves of the KTP/C applied in SMHBs in different cycles; and c) cycling performance of the KTP/C-based SMHBs.

the excellent ion transmission, and obtains ideal advancement in electrochemical kinetics. When the cell was tested under the low voltage window that reached 0.01 V, the plateau at  $\approx 0.5 \text{ V}$  remains unchanged in the following cycles, indicating excellent structural stability even under such a low voltage, which means that the capacity is dominated by intercalation reaction rather than conversion reaction. This result ensures the application of KTP/C in high voltage full cells, and as expected, it obtains an energy density of more than  $300 \text{ Wh kg}^{-1}$  (calculated using the average voltage times the capacity based on the mass of KTP/C) under the voltage window of 0.5–3.4 V, which is two to three times higher than the energy density ( $\approx 90 \text{ Wh kg}^{-1}$ ) under the normal voltage window (0.5–2.0 V). The two reversible intercalation reactions based plateaus of KTP/C endow its limitless development in the future.

### 3. Conclusion

In summary, the carbon coated  $\text{KTi}_2(\text{PO}_4)_3$  nanoparticle composite has been designed and successfully synthesized via a facile method. As the electrode material measured in SIB half cells, it exhibits a considerable capacity of  $104 \text{ mAh g}^{-1}$  with a flat voltage plateau at 2.1 V. Notably, a high capacity of  $76 \text{ mAh g}^{-1}$  is remained under an ultrahigh rate of 100 C. In

addition, the intercalation reaction is confirmed when the cell was cycled under the low voltage windows that reached 0.01 V. Besides, the composite shows high energy density of more than 300 Wh kg<sup>-1</sup> when applied as the anode material in the full cell sodium ion battery. Furthermore, the composite also obtains good performances (63 mAh g<sup>-1</sup> with voltage plateaus at 1.3 V) as the cathode material in sodium-magnesium hybrid batteries. The synergy of large ion diffusion channel and fast electron transfer ensures superior electrochemical performances of the carbon-coated KTi<sub>2</sub>(PO<sub>4</sub>)<sub>3</sub> nanoparticle composite. The results above demonstrate the great development potential of the KTi<sub>2</sub>(PO<sub>4</sub>)<sub>3</sub> nanoparticles/carbon composite for sodium ion storage in the future.

#### 4. Experimental Section

All the reagents used in the experiment were of analytical grade and used without further purification.

**Sample Preparation:** For a typical synthesis, KTi<sub>2</sub>(PO<sub>4</sub>)<sub>3</sub>/carbon nanoparticles were synthesized by a co-precipitation method followed by the annealing process. 3 mmol phosphoric acid (H<sub>3</sub>PO<sub>4</sub>) was dissolved in a mixture of 30 mL ethanol (C<sub>2</sub>H<sub>5</sub>OH) and 30 mL ethylene glycol followed by stirring for 30 min. Then, 1 mmol potassium acetate (CH<sub>3</sub>COOK) and 2 mmol tetrabutyl titanate were sequentially added into the above solution. After that, the suspension was stirred vigorously over 2 h. This white precursor was collected by centrifugation and washed with ethanol for twice, and dried at 70 °C for 12 h in air. Finally, the precursor was annealed in Ar at 750 °C for 2 h with a heating rate of 5 °C min<sup>-1</sup> to obtain the black KTi<sub>2</sub>(PO<sub>4</sub>)<sub>3</sub>/carbon nanoparticles (noted as KTP/C). When the suspension was centrifuged and washed with deionized water and ethanol for several times, and dried at 70 °C for 12 h in air followed by annealing in air at 750 °C for 3 h with a heating rate of 5 °C min<sup>-1</sup>, the white KTi<sub>2</sub>(PO<sub>4</sub>)<sub>3</sub> nanoparticles (noted as KTP) were obtained.

To obtain the graphene wrapped KTi<sub>2</sub>(PO<sub>4</sub>)<sub>3</sub> nanoparticles (noted as KTP/G), 0.1 g KTP were dispersed in 1 mL of graphene (≈7 mg mL<sup>-1</sup>) solution by an ultrasonic process and the mixture was stirred vigorously for 6 h. After that, the mixture was dried directly at 70 °C for 12 h in air to get the gray KTP/G nanoparticles. The graphene was synthesized by a modified Hummers method.<sup>[8]</sup>

To obtain the carbon-coated Na<sub>3</sub>V<sub>2</sub>(PO<sub>4</sub>)<sub>3</sub> bulk (noted as NVP/C), 2 mmol acetylacetonate was dissolved in 30 mL ethanol at 80 °C in water bath. After that, 1.5 mmol sodium carbonate (Na<sub>2</sub>CO<sub>3</sub>) and 3 mmol ammonium dihydrogen phosphate (NH<sub>4</sub>H<sub>2</sub>PO<sub>4</sub>) were sequentially added into the above yellow suspension. Then, the white mixture was stirred vigorously for 6 h and dried directly at 70 °C over 12 h in air. Finally, the black NVP/C bulk was obtained by following annealing in Ar at 750 °C for 8 h with a heating rate of 3 °C min<sup>-1</sup>.

**Materials Characterization:** XRD was employed to characterize the crystallographic information using a Bruker D8 Advance X-ray diffractometer with a nonmonochromated Cu Ka X-ray source. Scanning electron microscopic (SEM) images and energy dispersive X-ray spectra (EDS) were collected with a JEOL-7100F SEM/EDS microscope at an acceleration voltage of 20 kV. TEM and high-resolution transmission electron microscopic (HRTEM) images were recorded by using a JEM-2100F STEM/EDS microscope. BET surface areas were measured using a Tristar II 3020 instrument by adsorption of nitrogen at 77 K. XPS measurement was performed using a VG Multi Lab 2000 instrument. TG/DSC was performed using a Netzsch STA 449C simultaneous thermal analyzer at a heating rate of 10 °C min<sup>-1</sup> in air.

**Measurements of Electrochemical Performances:** The electrochemical properties were evaluated by assembly of 2016 coin cells in a glove box filled with pure argon gas. In sodium half cells, sodium metal was used as the anode. 1 M solution of NaClO<sub>4</sub> in ethylene carbon-dimethyl carbonate (1 : 1 w/w) with 5% fluoroethylene carbonate (FEC) was used

as the electrolyte, and a Whatman glass fiber (GF/D) was used as the separator. The electrolyte used in SMHBs was prepared on the basis of the reported method.<sup>[25]</sup> The electrodes were produced from a mixed clay with a weight ratio of 60% KTi<sub>2</sub>(PO<sub>4</sub>)<sub>3</sub>/carbon active material, 30% acetylene black, and 10% polytetrafluoroethylene (PTFE). The mixed clay was rolled using a roller mill to form a freestanding film and was cut into slices and dried in an oven for 12 h at 70 °C. The loading mass of the active material was ≈2.0–4.0 mg cm<sup>-2</sup>. Galvanostatic charge–discharge measurement was performed using a multichannel battery testing system (LAND CT2001A). CV curves and EIS were recorded with an electrochemical workstation under the alternating current ranging from 0.01 Hz to 10 kHz (Autolab PGSTAT 302).

#### Supporting Information

Supporting Information is available from the Wiley Online Library or from the author.

#### Acknowledgements

J.Z.S. and C.P. contributed equally to this work. This work was supported by the National Key Research and Development Program of China (2016YFA0202603), the National Basic Research Program of China (2013CB934103), the National Natural Science Foundation of China (51521001 and 51602239), the National Natural Science Fund for Distinguished Young Scholars (51425204), and the Fundamental Research Funds for the Central Universities (WUT: 2016III001, 2016III003, and 2016IVA090). Prof. L.Q.M. gratefully acknowledges financial support from the China Scholarship Council (No. 201606955096).

#### Conflict of Interest

The authors declare no conflict of interest.

#### Keywords

KTi<sub>2</sub>(PO<sub>4</sub>)<sub>3</sub>, NASICON, sodium ion batteries, sodium-magnesium hybrid batteries

Received: January 25, 2017

Revised: March 15, 2017

Published online:

- [1] K. S. Wook, S. D. Hwa, X. Ma, C. Gerbr, K. Kang, *Adv. Energy Mater.* **2012**, *2*, 710.
- [2] V. N. Richard, *Nature* **2014**, *507*, 26.
- [3] M. D. Slater, D. Kim, E. Lee, C. S. Johnson, *Adv. Funct. Mater.* **2013**, *23*, 947.
- [4] L. Xia, S. Wang, G. Liu, L. Ding, D. Li, H. Wang, S. Qiao, *Small* **2016**, *12*, 853.
- [5] H. Pan, Y. Hu, L. Chen, *Energy Environ. Sci.* **2013**, *6*, 2338.
- [6] Y. Wang, J. Yang, S. Chou, H. Liu, W. Zhang, D. Zhao, S. Dou, *Nat. Commun.* **2015**, *6*, 8689.
- [7] D. Su, A. McDonagh, S. Qiao, G. Wang, *Adv. Mater.* **2017**, *29*, 1604007.
- [8] D. Chao, C. Zhu, X. Xia, J. Liu, X. Zhang, J. Wang, P. Liang, J. Lin, H. Zhang, Z. Shen, H. Fan, *Nano Lett.* **2015**, *15*, 565.
- [9] M. S. Whittingham, *ChemInform* **2015**, *114*, 11414.

- [10] Y. Xu, Q. Wei, C. Xu, Q. Li, Q. An, P. Zhang, J. Sheng, L. Zhou, L. Mai, *Adv. Energy Mater.* **2016**, *6*, 1600389.
- [11] A. R. Armstrong, C. Lyness, P. M. Panchmatia, M. S. Islam, P. G. Bruce, *Nat. Mater.* **2011**, *10*, 223.
- [12] K. M. Hercule, Q. Wei, O. K. Asare, L. Qu, A. M. Khan, M. Yan, C. Du, W. Chen, L. Mai, *Adv. Energy Mater.* **2015**, *5*, 1500060.
- [13] J. Sheng, H. Zang, C. Tang, Q. An, Q. Wei, G. Zhang, L. Chen, C. Peng, L. Mai, *Nano Energy* **2016**, *24*, 130.
- [14] Z. Jian, W. Han, X. Lu, H. Yang, Y. Hu, J. Zhou, Z. Zhou, J. Li, W. Chen, D. Chen, L. Chen, *Adv. Energy Mater.* **2013**, *3*, 156.
- [15] C. Wu, P. Kopold, Y. Ding, P. A. van Aken, J. Maier, Y. Yu, *ACS Nano* **2015**, *9*, 6610.
- [16] Y. Fang, L. Xiao, J. Qian, Y. Cao, X. Ai, Y. Huang, H. Yang, *Adv. Energy Mater.* **2016**, *6*, 1502197.
- [17] C. Xu, Y. Xu, C. Tang, Q. Wei, J. Meng, L. Huang, L. Zhou, G. Zhang, L. He, L. Mai, *Nano Energy* **2016**, *28*, 224.
- [18] J. Han, Y. Niu, S. Bao, Y. Yu, S. Lu, M. Xu, *Chem. Commun.* **2016**, *52*, 11661.
- [19] J. Han, M. Xu, Y. Niu, M. Jia, T. Liu, C. Li, *J. Colloid Interface Sci.* **2016**, *483*, 67.
- [20] H. D. Yoo, I. Shterenberg, Y. Gofer, G. Gershinsky, N. Pour, D. Aurbach, *Energy Environ. Sci.* **2013**, *6*, 2265.
- [21] X. Sun, V. Duffort, B. L. Mehdi, N. D. Browning, L. F. Nazar, *Chem. Mater.* **2015**, *128*, 44.
- [22] Q. An, Y. Li, H. D. Yoo, S. Chen, Q. Rua, L. Mai, Y. Yao, *Nano Energy* **2015**, *18*, 265.
- [23] T. Ichitsubo, T. Adachi, S. Yagi, T. Doi, *J. Mater. Chem.* **2011**, *21*, 11764.
- [24] X. Sun, V. Duffort, L. F. Nazar, *Adv. Sci.* **2016**, *3*, 1600044.
- [25] S. Su, Y. Nuli, Z. Huang, Q. Miao, J. Yang, J. Wang, *ACS Appl. Mater. Interfaces* **2016**, *8*, 7111.
- [26] Y. Cheng, Y. Shao, J. Zhang, V. L. Sprenkle, J. Liu, G. Li, *Chem. Commun.* **2014**, *50*, 9644.
- [27] H. Dong, Y. Li, Y. Liang, G. Li, C. Sun, Y. Ren, Y. Lu, Y. Yao, *Chem. Commun.* **2016**, *52*, 8263.
- [28] X. Bian, Y. Gao, Q. Fu, S. Indris, Y. Ju, Y. Meng, F. Du, N. Bramnik, H. Ehrenberg, Y. Wei, *J. Mater. Chem. A* **2017**, *5*, 600.
- [29] W. Han, G. Zhao, X. Zhang, S. Zhou, P. Wang, Y. An, B. Xu, *Carbon* **2015**, *95*, 157.
- [30] C. Han, M. Yan, L. Mai, X. Tian, L. Xu, X. Xua, Q. An, Y. Zhao, X. Ma, J. Xie, *Nano Energy* **2013**, *2*, 916.
- [31] Z. Cai, L. Xu, M. Yan, C. Han, L. He, K. M. Hercule, C. Niu, Z. Yuan, W. Xu, L. Qu, K. Zhao, L. Mai, *Nano Lett.* **2015**, *15*, 738.
- [32] A. R. Burke, C. R. Brown, W. C. Bowling, J. E. Glaub, D. Kapsch, C. M. Love, R. B. Whitaker, W. E. Moddeman, *Surf. Interface Anal.* **1988**, *11*, 353.
- [33] V. D. Klimov, A. A. Vashman, I. S. Pronin, *Zh. Obshch. Khim.* **1991**, *61*, 2166.
- [34] P. Moreau, G. Ouvrard, P. Gressier, P. Ganal, J. Rouxel, *J. Phys. Chem. Solids* **1996**, *57*, 1117.
- [35] L. Hernan, J. Morales, L. Sanches, J. L. Tirado, J. P. Espinos, A. R. Gonzalez Elipe, *Chem. Mater.* **1995**, *7*, 1576.
- [36] P. Senguttuvan, G. Rousse, M. E. A. Dompablo, H. Vezin, J. M. Tarascon, M. R. Palacin, *J. Am. Chem. Soc.* **2013**, *135*, 3897.
- [37] D. Wang, Q. Liu, C. Chen, M. Li, X. Meng, X. Bie, Y. Wei, Y. Huang, F. Du, C. Wang, G. Chen, *ACS Appl. Mater. Interfaces* **2016**, *8*, 2238.
- [38] X. Yu, H. Pan, W. Wan, C. Ma, J. Bai, Q. Meng, S. N. Ehrlich, Y.-S. Hu, X.-Q. Yang, *Nano Lett.* **2013**, *13*, 4721.